# Pulmonary Embolism Detecton using Localized Vessel–Based Features in Dual Energy CT

Yashin Dicente Cid[ab], Adrien Depeursinge[a], Antonio Foncubierta–Rodríguez[a], Alexandra Platon[b], Pierre–Alexandre Poletti[b] and Henning Müller[ab]

[a]University of Applied Sciences Western Switzerland (HES–SO), Sierre, Switzerland;
[b]University Hospitals and University of Geneva, Geneva, Switzerland

## ABSTRACT

Pulmonary embolism (PE) affects up to 600,000 patients and contributes to at least 100,000 deaths every year in the United States alone. Diagnosis of PE can be difficult as most symptoms are unspecific and early diagnosis is essential for successful treatment. Computed Tomography (CT) images can show morphological anomalies that suggest the existance of PE. Various image–based procedures have been proposed for improving computer–aided diagnosis of PE. We propose a novel method for detecting PE based on localized vessel–based features computed in Dual Energy CT (DECT) images. DECT provides 4D data indexed by the three spatial coordinates and the energy level. The proposed features encode the variation of the Hounsfield Units across the different levels and the CT attenuation related to the amount of iodine contrast in each vessel. A local classification of the vessels is obtained through the classification of these features. Moreover, the localization of the vessel in the lung provides better comparison between patients. Results show that the simple features designed are able to classify pulmonary embolism patients with an AUC (area under the receiver operating curve) of 0.71 on a lobe basis. Prior segmentation of the lung lobes is not necessary because an automatic atlas–based segmentation obtains similar AUC levels (0.65) for the same dataset. The automatic atlas reaches 0.80 AUC in a larger dataset with more control cases.

**Keywords:** Dual Energy CT, Pulmonary Embolism, 4D analysis

## 1. INTRODUCTION

Acute pulmonary embolism (PE) is a common condition that consists of the obstruction of one or more arteries in the lungs as a complication of deep vein thrombosis (DVT). Studies evidenced that acute PE mortality rates can reach 75% during initial hospital admission[1] and 30% within 3 years after the hospital discharge.[2] Although it can be successfully treated with anticoagulants, delays in diagnosis have shown to increase the risk of death.[3]

Schickert et al.[4] confirmed that Computed Tomography (CT) image analysis allows detection of chronic thromboembolism. 3D texture information is relevant to quantify pulmonary parenchyma ischemia in CT imaging.[5] Recently Dual Energy CT (DECT) was shown to allow quantifying perfusion defects of the lung parenchyma[6–10] using iodine components derived from CT attenuation at two energy levels of 80 and 140 keV. Post–processing of DECT images permits isolating iodine components from other attenuations caused by anatomical structures. Therefore, accurate local quantification of the blood flow can be obtained and was investigated for various applications. Foncubierta–Rodríguez et al.[11] used the 4D data contained in DECT images for enhanced visualization of pulmonary perfusion using a color coded overlay. Moreover, other studies focused into analyzing the 3.5–D texture of the DECT images by combining the 3D texture in the different energy levels.[12–14] All these studies tried to detect the disease by analyzing the texture of the lung without distinguishing patterns present in the parenchyma from patterns found in the vascular structure of the lung. Therefore, these approaches are prone to information loss due to the unspecificity of the patterns analyzed.

In this paper a novel approach focused on the vessels of the lung is presented. Features that combine energy attenuation and spatial information are used to predict the existence of PE. These features are computed

Further author information: (Send correspondence to Y.D.C.)
Y.D.C., Email: yashin.dicente@hevs.ch

in automatically extracted anatomical lung regions. Results show that the proposed features contain enough information to locally predict the presence of PE. When compared to previous studies, the proposed approach requires no lobe segmentation, allowing to obtain fully automatic predictions.

## 2. METHODS

This section describes the details concerning the dataset and the techniques employed to carry out the experiments.

### 2.1 Dataset

Experiments were made on chest DECT images of 38 patients, 18 of them with proven PE and 20 control cases (CC). DECT images were obtained with a Discovery CT750 HD machine from General Electric Medical Systems.

Dataset–1 is a subset consisting of the 18 PE patients and 8 CC. The lung lobes of these patients were manually segmented by a medical doctor. The Qanadli index[15] was manually computed for each lobe of the 26 patients in Dataset–1. This index is used to quantify the degree of arterial obstruction in PE. Dataset–1 plus the 12 CC with no lobes segmentation is considered as Dataset–2. The Qanadli index on these 12 CC is assumed to be 0 in the full lungs. 11 energy levels were chosen from each DECT image (4–D image), from 40 KeV to 140 KeV in steps of 10 KeV.

### 2.2 Atlas of the lung

The features presented in this paper focus on the information inside the vessels, but this information may vary with the size of the vessel. Therefore, an atlas–based segmentation in regions with similar vessels size was selected. This atlas, proposed by Depeursinge et al.,[16] allows to compare vessel properties in similar localization between patients. Moreover, this atlas can be computed fully automatically because it relies on the geometry of the lung, and no human interaction is needed. The atlas contains 36 region produced by intersecting 4 axis segmentations. For a better identification, the 36 regions where labeled with a 4 letter code according to the axis segmentation. The order of the letters and their meaning are shown in Figure 1. E.g., the region 'LACM' corresponds to the Left lung–Anterior–Central–Middle region. The vertical segmentation was refined to obtain a balanced distribution of regions. The new approach computed the height of the lung using the distance between the highest point (apex) and the mean of the points of the base of the lung. This refinement produced more proportional vertical regions (see Figure 2). A value was assigned to each region based on the Qanadli index of the lobes intersected by the region. This approximation to a Qanadli index by region was used as an indicator of PE.

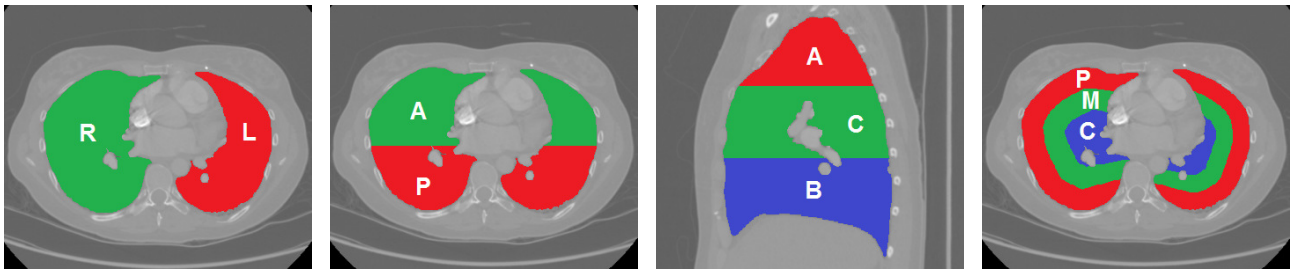


Coronal segmentation: **R**ight, **L**eft | Sagital segmentation: **A**nterior, **P**osterior | Vertical segmentation: **A**pical, **C**entral, **B**asal | Axial segmentation: **P**eripheral, **M**idle, **C**entral

Figure 1. Atlas–based segmentation presented by Depeursinge et al.[16] The atlas is built by dividing the lungs geometrically along 4 axes. The intersection of these divisions form the 36 regions of the atlas. The final regions were labeled with a 4–letters code placed in the order shown above and encode the position of the region in the corresponding axis.

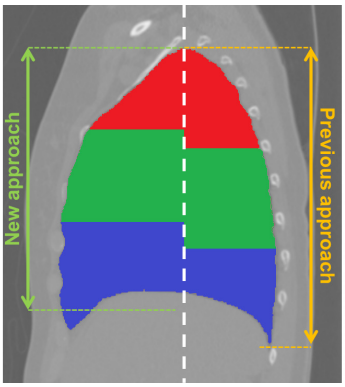


Figure 2. Refined atlas segmentation for the vertical regions. In this work a vertical segmentation considering the shape of the lung is presented, and obtains more proportional regions than only considering the vertical size.

### 2.3 Features: energy–based prisms

The features were designed to encode the variation of the Hounsfield Units (HU) across the 11 energy levels and the attenuation caused by the iodine contrast in each vessel, combining the information of the 4 dimensions of the DECT image. The 140 KeV energy level was selected to segment the vessels thanks to its stability. Then, given a CT axial slice from the 140 KeV energy level, the vessels of the lungs were segmented by an appropriate threshold, obtaining a mask of the vessels (see Figure 3). This threshold was experimentally fixed to preserve the largest number of vessels, i.e. preserving the small vessels in the peripheral regions of the lung. A *vessel axial section* $Vs \subset \mathbb{R}^2$ is defined as a connected component of the mask obtained for a given CT slice. Let $HU_i(p)$ be the HU for a given point $p \in Vs$, in the $i \in \{1, \cdots, 11\}$ energy level (see Section 2.1). Then, a *Vs–prism* $V$ is defined as:

$$V = \left\{ \Big( p, (HU_1(p), \cdots, HU_{11}(p)) \Big) \mid p \in Vs, HU_i : Vs \to \mathbb{R} \right\}$$

Figure 4 illustrates the construction of a *Vs*–prism.

Let $\mathcal{V}$ be the set of *Vs*–prisms $V$. Then, the following function $f$ defines the feature vector of a given *Vs*–prism:

$$\begin{array}{rccc} f: & \mathcal{V} \to & & \mathbb{R}^{11} \\ & V \mapsto & \left( \frac{\sum_{p \in Vs} HU_1(p)}{|Vs|}, \cdots, \frac{\sum_{p \in Vs} HU_{11}(p)}{|Vs|} \right) & \end{array}$$

where $|Vs|$ is the cardinality of $Vs$.

### 2.4 *Vs*–prism classification

The number of *Vs*–prisms classified as healthy class in a given region allows to locally estimate the perfusion in that region. The more *Vs*–prisms are classified as healthy class, the healthiest is the region.

On average, 24,780 *Vs*–prisms and 27,068 *Vs*–prisms per patient were obtained in the lobe–based and in the atlas–based segmentation respectively. The small difference in average between both segmentations comes from the geometrical segmentation of the lung in atlas regions where some vessels were split. The distribution of the number of *Vs*–prisms in the different regions is shown in Table 1 and in Table 2 respectively.

A one–class support vector machine (SVM) classifier was used to model the healthy class and provide decisions for each *Vs*–prism in each region. Since it can not be assumed that all *Vs*–prisms in a region of the PE patients were equally affected, the non–healthy class could not be modeled. Because of this heterogeneous distribution, only the *Vs*–prisms of fully healthy patients were considered to train the healthy class (i.e. those patients with a Qanadli index equal to 0 in the full lung). Healthy regions in patients with PE were not used to train the classifier.

| Lobe | % |
|---|---|
| RU | 26.61 |
| RM | 8.66 |
| RL | 20.40 |
| LU | 28.25 |
| LL | 16.08 |

Table 1. Distribution of the *Vs*–prisms by lobe in the lobe–based segmentation. The values are related to the size of the lobes.

| Region | % | Region | % | Region | % | Region | % |
|---|---|---|---|---|---|---|---|
| RAAC | 0.27 | RPAC | 0.36 | LAAC | 0.58 | LPAC | 0.65 |
| RAAM | 1.29 | RPAM | 2.14 | LAAM | 1.56 | LPAM | 2.17 |
| RAAP | 2.32 | RPAP | 3.58 | LAAP | 2.81 | LPAP | 3.88 |
| RACC | 1.17 | RPCC | 1.20 | LACC | 1.65 | LPCC | 1.01 |
| RACM | 3.22 | RPCM | 4.09 | LACM | 3.37 | LPCM | 2.98 |
| RACP | 4.50 | RPCP | 5.37 | LACP | 5.79 | LPCP | 5.01 |
| RABC | 1.75 | RPBC | 2.20 | LABC | 0.74 | LPBC | 1.68 |
| RABM | 2.89 | RPBM | 4.61 | LABM | 1.60 | LPBM | 3.38 |
| RABP | 5.08 | RPBP | 6.77 | LABP | 3.68 | LPBP | 4.66 |

Table 2. Distribution of the *Vs*–prisms by atlas region. The mean proportion of *Vs*–prisms per region is 2.78% (100% divided by 36 regions).

The classification was done at the region–level because vessel size depends on the lung location, affecting the size of the *Vs*–prisms. This region–based classification allowed to compare *Vs*–prisms with similar size.

### 2.5 Validation

The proposed validation system was composed of three main steps: random selection of training patients to build a model, optimization of the SVM parameters for the obtained model, and evaluation of the performance in a test set. This process was repeated 10 times in order to reduce the effect of the random selection of the training set. As a one–class SVM classifier was used, only the parameter $\gamma$ was optimized. Each model was created by randomly selecting 75% of the CC and 50% of the PE patients. The remaining patients, 25% of CC and 50% of PE, constituted the test set for this model. The optimization of the SVM parameter $\gamma$ was performed with a leave–one–patient–out (LOPO) cross–validation. Only the *Vs*–prisms of healthy patients were considered for the training (see Section 2.4). The validation of the LOPO cross–validation was performed in all the patients of the model. The $\gamma$ obtained in the optimization step and all the CC selected in the model were used to build the final SVM training model, and the final performance was computed on the corresponding test set.

In each repetition of the validation system, the selected $\gamma$ can differ because of the random selection of the training patients that compose the model. In Section 3, the final performance shown is the mean performance of the models with the most frequently repeated $\gamma$. For Dataset–1, the models contain 6 CC and 9 PE patients, while the test sets contain 2 CC and 9 PE patient. In the case of Dataset–2, the models contain 15 CC and 9 PE patients and in this case the test sets contain 5 CC and 9 PE patients.

## 3. RESULTS

The area under the receiver operating curve (AUC) was used to measure the classification performance for each region. The mean of the AUCs and the weighted mean taking into account the percentage of *Vs*–prisms per region, as detailed in Section 2.4, were also computed to obtain an overall measurement for all regions.

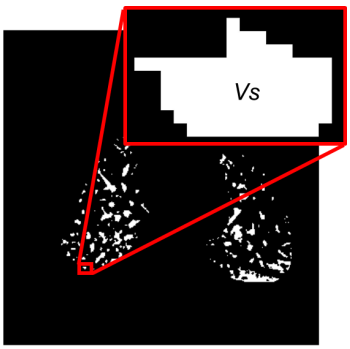


Figure 3. Vessel mask of a CT axial slice keeping the small peripheral vessels. A connected component *Vs* is emphasized for understanding *Vs*–prisms construction illustrated in Figure 4.

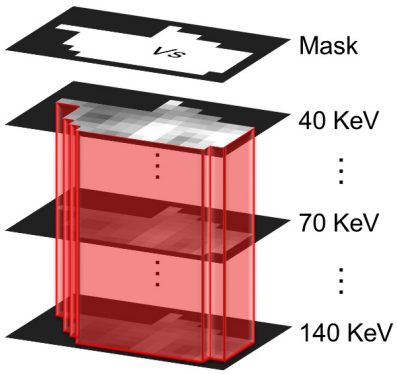


Figure 4. Graphical construction of a *Vs*–prism from a vessel section *Vs* and the 11 energy levels. The mask presented shows the shape of the connected component.

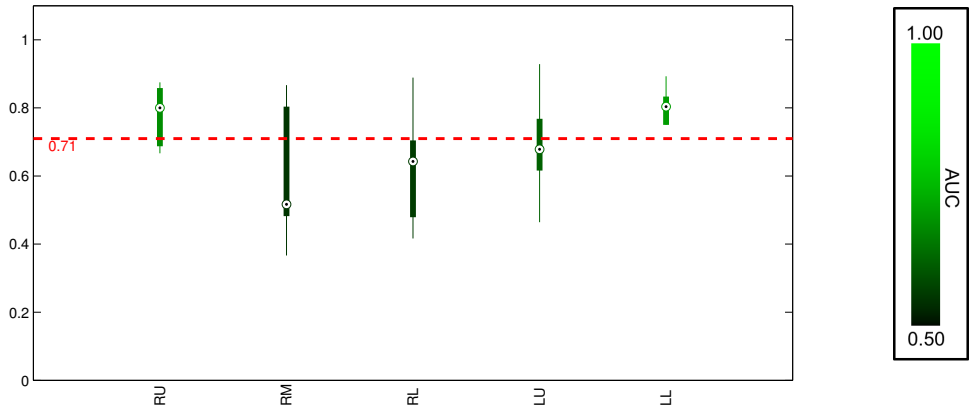


**Mean AUC = 0.70**
**Weighted mean AUC = 0.71**

Figure 5. Mean AUC by lobe in the Dataset–1 using the lobe–based segmentation and the corresponding variance due to the random selection of patients that composes the validation models (see Section 2.5). The red line indicates the weighted mean AUC obtained by considering the proportion of *Vs*–prisms by lobe detailed in Table 1.

### 3.1 Dataset–1

Figure 5 shows the mean AUC per lobe in the lobe–based segmentation and the variance obtained in the validation step, explained in Section 2.5. The mean value per lobe is always above 0.5. The overall mean is 0.70 AUC, but considering the proportion of *Vs*–prisms per lobe presented in Table 1, the overall weighted mean is 0.71 AUC. The lowest AUC and the highest variance are obtained in the right middle lobe (RM) because its low proportion of *Vs*–prisms (see Table 1). In Figure 6 (left) it can be observed the size of every lobe and the performance in a green scale code, where light green denotes an AUC of 1, and fully black is an AUC of 0.5. For better understanding, an axial view of the 5 lobes is also shown in Figure 6 (right) with same color code for the AUC measure.

The performance per region for the atlas–based segmentation is shown in Figure 7. The variance of the performance for this segmentation is higher than for the lobe–based segmentation due to the low number of *Vs*–prisms per region (see Table 2). In this case, the mean AUC remains 0.60, while, considering the proportion

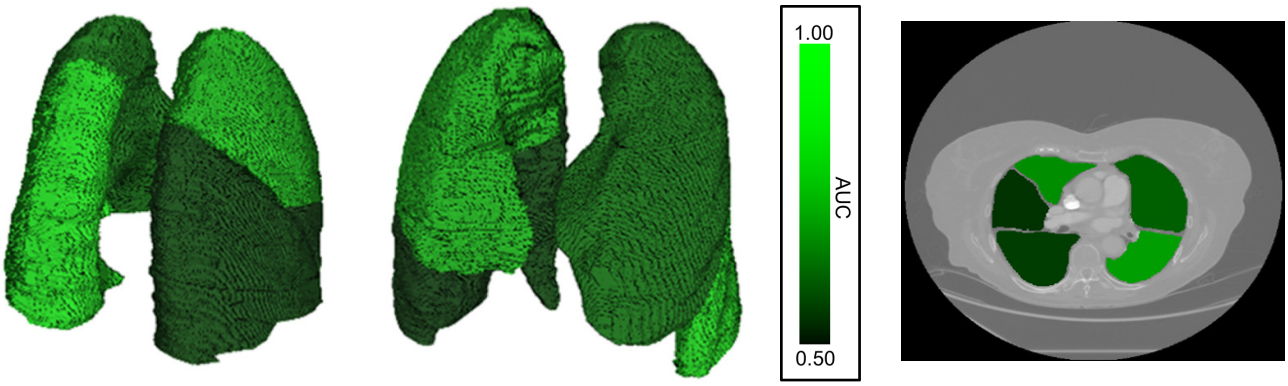


Figure 6. Posterior view and anterior view of a 3D visualization of the lobes, painted in a green scale corresponding to the mean AUC obtained by lobe. An axial slice with the 5 lobes is also provided with the same green scale. These two visualizations illustrate the size of each lobe and help understanding the heterogeneous distribution of *Vs*–prisms shown in Table 1.

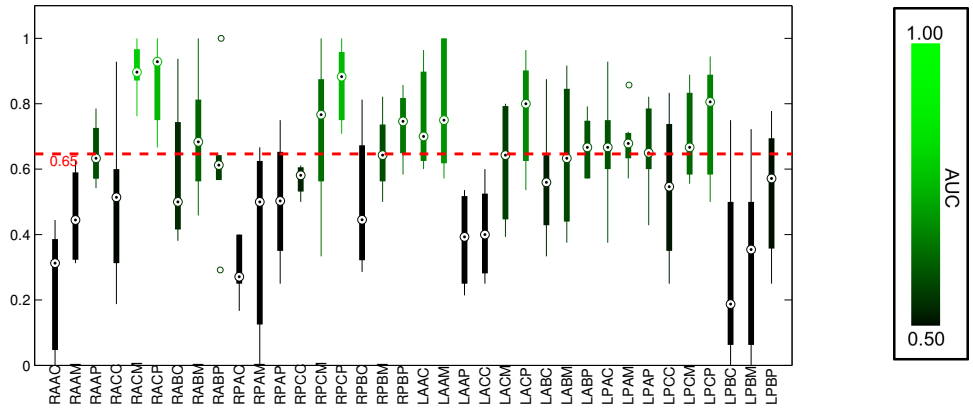


**Mean AUC = 0.60**
**Weighted mean AUC = 0.65**

Figure 7. Mean AUC by region in Dataset–1 using the atlas–based segmentation and its variance due to the validation step explained in Section 2.5. Regions with low mean AUC and high variance are those with fewer *Vs*–prisms, as shown in Table 2. The weighted mean AUC of the regions considering this distribution of *Vs*–prisms is marked in red. The values are less stable than in the lobe–based segmentation because of the segmentation of the lungs into 36 regions and, as a consequence, their small number of *Vs*–prisms with respect to the number of *Vs*–prisms per lobe.

of *Vs*–prisms, the weighted AUC reaches 0.65. Again, the regions with lower performance are those ones with fewer *Vs*–prisms. The 3D visualization of the AUC per region presented in Figure 8 can not show the 36 regions, but illustrates the localization of the atlas regions. The green scale used is the same than in previous figures and the 2D visualization of the performance in the same Figure 8 needs 3 axial slices to show the 36 regions.

The results in Dataset–1 for the lobe–based segmentation had similar performance as the atlas–based seg-

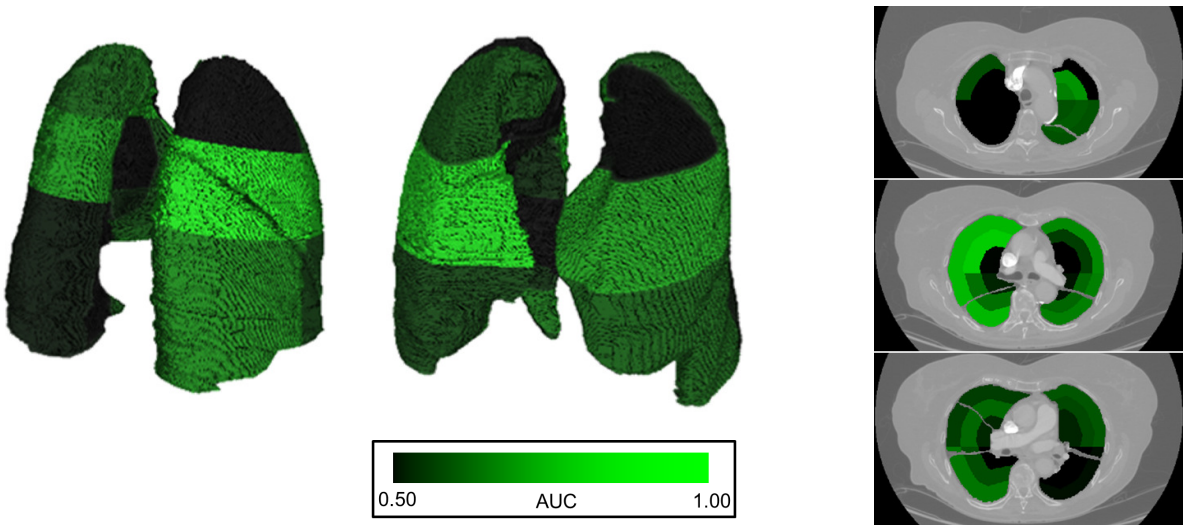


Figure 8. Posterior view and anterior view of a 3D visualization of the lungs with the different regions of the atlas painted with the same green scale as previous figures for showing the performance in Dataset–1. In combination with the 3 axial slides provided the size and the localization of the 36 regions can be observed. The performance is even higher than for the lobe–based segmentation in the central–peripheral regions considering the vertical and axial segmentations respectively (see Figure 1). These regions are the ones with more *Vs*–prisms (see Table 2) because they are the biggest ones.

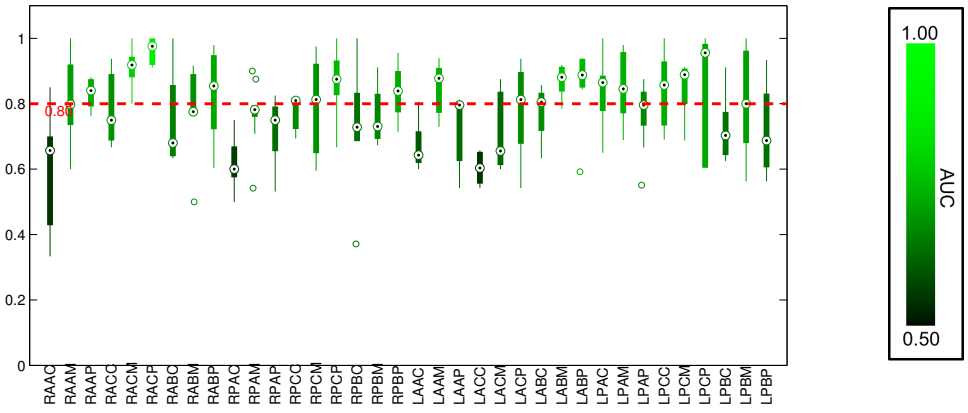


**Mean AUC = 0.78**
**Weighted mean AUC = 0.80**

Figure 9. On Dataset–2, the mean weighted AUC (red line) reached 0.80 and the variance in each region of the atlas is considerably reduced. Except for 3 regions, the AUC per region is over 0.60, even considering its variance. In this second dataset there are more *Vs*–prisms of the reference class per region. This stabilizes and increases the performance, showing that the designed features describe the healthy class well.

mentation on the same dataset. It can be observed that the regions with lowest performance (low mean AUC and high variance) are the regions with fewer *Vs*–prisms in both segmentations.

### 3.2 Dataset–2

Figure 9 shows a large increment of the mean AUC per region and a high reduction of the variance in all regions. In this case, the mean AUC is 0.78 and the weighted mean AUC reaches 0.80 considering again the distribution of the *Vs*–prisms (see Table 2). The performance per region in Dataset–2 is above 0.5 in all regions. The 3D

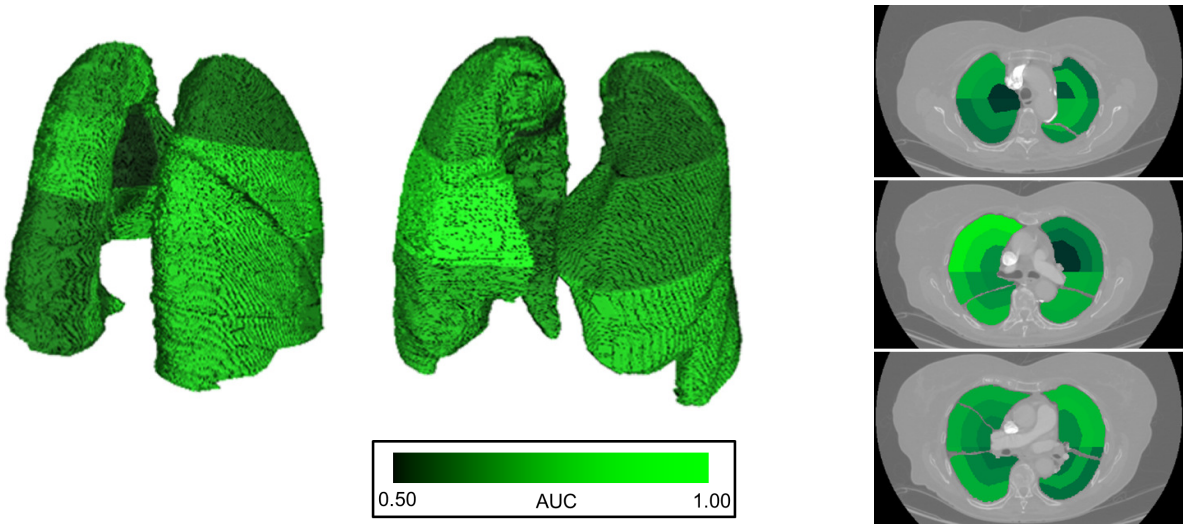


Figure 10. The same information is provided for Dataset–2 as for Dataset–1 in Figure 8 . The high improvement of the smallest regions can be observed clearly. However, some small regions in the center of the lung still have low AUC. These are the regions with less than 0.6% *Vs*–prisms in Table 2.

and 2D visualizations in Figure 6 clearly show this high improvement in all regions. The same green scale as in Dataset–1 figures is used for presenting the mean AUC per region.

The number of healthy *Vs*–prisms per region in the training set of this dataset was increased and it had a direct influence in the stability of the final performance. Moreover, the newly added control cases enriched the reference class (healthy class) resulting in an important improvement of the final performance, increasing the mean AUC per region and reducing its variance across the models used in the validation.

## 4. DISCUSSION

Experiments on Dataset–1, based on the lobe–based and on the atlas–based segmentations, show that these two segmentations obtained similar results. As the atlas is computed fully automatically, no human interaction is needed to obtain similar performance as with the lobe–based segmentation carried out by an expert medical doctor. The poorest results on the atlas–based segmentation derive from the low number of *Vs*–prisms obtained per region because of the fine segmentation of the lungs into 36 regions. The mean percentage of *Vs*–prisms per region is 20% and 2.78% in the lobe–based and atlas–based segmentations respectively (see Table 2). By considering only those regions with a proportion of *Vs*–prisms close to the mean percentage, equivalent performance is obtained between both segmentations. The variance of these region also reaches the lowest values (see Figure 7).

The third experiment on Dataset–2 was performed with the hypothesis that the AUC was affected by the number of healthy *Vs*–prisms used for training in each region. In this case results show an important overall increment but considering this time regions with fewer *Vs*–prisms (see Table 2), this increment is even higher.

The variance of the performance obtained, because of the validation step (see Section 2.5), behaves in the same way, obtaining a final variance much lower than for Dataset–1 with the same segmentation.

The lobe–based segmentation was provided only for 8 CC and, in order to avoid overfitting, this small set had to be split into training and testing sets when evaluating the performance of the methods. Standard settings often select 50% of the patients for training but large inter–patient variability in Dataset–1 seriously affected the creation of a healthy class with only 4 patients. This variability forced us to create a more complex validation process to compute a reliable performance of the classification. The process presented in Section 2.5 is able to deal with datasets with a small number of elements for each class. The proportions of patients in the selection of the models were designed to keep enough information of the reference class (healthy) while keeping sufficient patients for a test set.

The results obtained in Dataset–2 with a higher stability of the parameter $\gamma$ selected by the optimization step also support the suitability of the validation system designed.

The selection of a one–class classifier was motivated by the heterogeneous distribution of the *Vs*–prisms in the lungs but it fits perfectly for unbalanced data such as Dataset–1.

## 5. CONCLUSIONS AND FUTURE WORK

In this paper new visual features are presented based on the vessel segmentation of DECT images that able to detect pulmonary embolism patients with a high accuracy. These features encode the information of the 4 dimensions in DECT in a single vector. The overall AUC values achieved are high taking into account the simplicity of the features presented and encourage the possibility that better performance can be achieved by just applying small improvements to the described techniques. Results also showed that a good performance is achieved using the atlas segmentation and no lobe segmentation is necessary to classify a new patient.

A new validation system was presented able to deal with an unbalance dataset with classes with few elements. The system provides information about the richness of the referenced class and avoids overfitting. Thanks to this extra information more reliable results were obtained.

The vessel segmentation proposed in this paper was based on a simple thresholding. Future work includes the use of other vessel segmentation techniques, such as, the one presented by Helmberger et al.[17] This vessel segmentation relies on the properties of the Hessian to model structures.

Another approach that should be tested is to combine the features presented with other features based on texture such as[18] using Riesz wavelets. This allows to leverage the local morphological properties of the parenchyma, which was shown to be an indicator of PE.[5,13]

## ACKNOWLEDGMENTS

This work was partly supported by the Swiss National Science Foundation in the PH4D project (grant agreement 320030–146804).

## REFERENCES

[1] S. Z. Goldhaber, L. Visani, and M. D. Rosa, "Acute pulmonary embolism: clinical outcomes in the international cooperative pulmonary embolism registry (icoper)," *The Lancet* **353**(9162), pp. 1386 – 1389, 1999.

[2] F. A. Anderson Jr., H. B. Wheeler, R. J. Goldberg, D. W. Hosmer, N. A. Patwardhan, B. Jovanovic, A. Forcier, and J. E. Dalen, "A population-based perspective of the hospital incidence and case-fatality rates of deep vein thrombosis and pulmonary embolism: The worcester dvt study," *Archives of Internal Medicine* **151**(5), pp. 933–938, 1991.

[3] S. Ozsu, F. Oztuna, Y. Bulbul, M. Topbas, T. Ozlu, P. Kosucu, and A. Ozsu, "The role of risk factors in delayed diagnosis of pulmonary embolism," *The American Journal of Emergency Medicine* **29**(1), pp. 26 – 32, 2011.

[4] H. C. Schwickert, F. Schweden, H. H. Schild, R. Piepenburg, C. Düber, H.-U. Kauczor, C. Renner, S. Iversen, and M. Thelen, "Pulmonary arteries and lung parenchyma in chronic pulmonary embolism: preoperative and postoperative CT findings.," *Radiology* **191**(2), pp. 351–357, 1994.

[5] B. Ganeshan, K. A. Miles, R. C. D. Young, and C. R. Chatwin, "Three–dimensional selective–scale texture analysis of computed tomography pulmonary angiograms," *Investigative Radiology* **43**, pp. 382–394, June 2008.

[6] E. J. Chae, J. B. Seo, Y. M. Jang, B. Krauß, C. W. Lee, H. J. Lee, and K.-S. Song, "Dual–energy CT for assessment of the severity of acute pulmonary embolism: Pulmonary perfusion defect score compared with CT angiographic obstruction score and right ventricular/left ventricular diameter ratio," *American Journal of Roentgenology* **194**(3), pp. 604–610, 2010.

[7] C. Lee, J. Seo, J.-W. Song, M.-Y. Kim, H. Lee, Y. Park, E. Chae, Y. Jang, N. Kim, and B. Krauß, "Evaluation of computer–aided detection and dual energy software in detection of peripheral pulmonary embolism on dual-energy pulmonary CT angiography," *European Radiology* **21**(1), pp. 54–62, 2011.

[8] S. F. Thieme, C. R. Becker, M. Hacker, K. Nikolaou, M. F. Reiser, and T. R. C. Johnson, "Dual energy CT for the assessment of lung perfusion—correlation to scintigraphy," *European Journal of Radiology* **68**(3), pp. 369–374, 2008.

[9] S. F. Thieme, T. R. Johnson, C. Lee, J. McWilliams, C. R. Becker, M. F. Reiser, and K. Nikolaou, "Dual-energy ct for the assessment of contrast material distribution in the pulmonary parenchyma," *American Journal of Roentgenology* **193**(1), pp. 144–149, 2009.

[10] T. Nakazawa, Y. Watanabe, Y. Hori, K. Kiso, M. Higashi, T. Itoh, and H. Naito, "Lung perfused blood volume images with dual–energy computed tomography for chronic thromboembolic pulmonary hypertension: Correlation to scintigraphy with single–photon emission computed tomography," *Journal of Computer Assisted Tomography* **35**(5), pp. 590–595, 2011.

[11] A. Foncubierta-Rodríguez, A. Widmer, A. Depeursinge, and H. Müller, "Enhanced visualization of pulmonary perfusion in 4d dual energy ct images," in *The 36th Annual International Conference of the IEEE Engineering in Medicine and Biology Conference (EMBC 2014)*, 2014.

[12] A. Foncubierta-Rodríguez, O. A. Jiménez del Toro, A. Platon, P.-A. Poletti, H. Müller, and A. Depeursinge, "Benefits of texture analysis of dual energy CT for computer–aided pulmonary embolism detection," in *The 35th Annual International Conference of the IEEE Engineering in Medicine and Biology Conference (EMBC 2013)*, 2013.

[13] A. Depeursinge, A. Foncubierta-Rodríguez, A. Vargas, D. Van De Ville, A. Platon, P.-A. Poletti, and H. Müller, "Rotation–covariant texture analysis of 4D dual–energy CT as an indicator of local pulmonary perfusion," in *IEEE 10th International Symposium on Biomedical Imaging*, *ISBI 2013*, pp. 149–152, IEEE, April 2013.

[14] A. Foncubierta-Rodríguez, P.-A. Poletti, A. Platon, A. Vargas, H. Müller, and A. Depeursinge, "Texture quantification in 4D dual energy CT for pulmonary embolism diagnosis," in *MICCAI workshop MCBR–CDS 2012*, *Springer LNCS* **7723**, pp. 45–56, 2013.

[15] S. D. Qanadli, M. El Hajjam, A. Vieillard-Baron, T. Joseph, B. Mesurolle, V. L. Oliva, O. Barré, F. Bruckert, O. Dubourg, and P. Lacombe, "New CT index to quantify arterial obstruction in pulmonary embolism," *American Journal of Roentgenology* **176**(6), pp. 1415–1420, 2001.

[16] A. Depeursinge, T. Zrimec, S. Busayarat, and H. Müller, "3D lung image retrieval using localized features," in *Medical Imaging 2011: Computer-Aided Diagnosis*, **7963**, p. 79632E, SPIE, February 2011.

[17] M. Helmberger, M. Urschler, M. Pienn, Z. Balint, A. Olschewski, and H. Bischof, "Pulmonary vascular tree segmentation from contrast-enhanced CT images," *CoRR* **abs/1304.7140**, 2013.

[18] A. Depeursinge, A. Foncubierta-Rodríguez, D. Van De Ville, and H. Müller, "Rotation–covariant texture learning using steerable Riesz wavelets," *IEEE Transactions on Image Processing* **23**, pp. 898–908, February 2014.